LAWRENCE
LIVERMORE
NATIONAL
LABORATORY

LLNL-TR-644455

Metal Artifact Reduction for CT-based Luggage Screening

S. S. Karimi, P. C. Cosman

October 1, 2013

Disclaimer

This document was prepared as an account of work sponsored by an agency of the United States government. Neither the United States government nor Lawrence Livermore National Security, LLC, nor any of their employees makes any warranty, expressed or implied, or assumes any legal liability or responsibility for the accuracy, completeness, or usefulness of any information, apparatus, product, or process disclosed, or represents that its use would not infringe privately owned rights. Reference herein to any specific commercial product, process, or service by trade name, trademark, manufacturer, or otherwise does not necessarily constitute or imply its endorsement, recommendation, or favoring by the United States government or Lawrence Livermore National Security, LLC. The views and opinions of authors expressed herein do not necessarily state or reflect those of the United States government or Lawrence Livermore National Security, LLC, and shall not be used for advertising or product endorsement purposes.

This work performed under the auspices of the U.S. Department of Energy by Lawrence Livermore National Laboratory under Contract DE-AC52-07NA27344.

image with a few values of λ and selected the value that gave the best visual result. In Eqn. (3), I_1 is an indicator function:

$$I_1(j) = \begin{cases} 1 & X_{Orig}(j) > M_1 \\ 0 & \text{otherwise.} \end{cases} \tag{4}$$

The threshold M_1 is set to 4000 Modified Hounsfield units (MHU). A voxel above this threshold is interpreted to contain metal or be close to metal. The MHU scale has an offset of 1000 relative to the conventional Hounsfield scale, so that water is 1000 MHU and air is zero. We use MHU rather than HU to simplify the summation.

The summation in Eqn. (3) represents the path length through metal of the ray that gives projection sample i. We choose an exponential weighting function because the attenuation of x-rays follows the Beer-Lambert law [2], and the weights are monotonic and smooth. $W_{X_{Orig}}$ is computed once per image and then is kept constant for the optimization problem. Therefore, although $W_{X_{Orig}}$ depends on the image, the first term in Eqn. (2) is quadratic.

The regularization term $||x||_{TV}$ is the total variation norm and β is its strength. The total variation norm is popular in compressive sensing, and it has been used for reconstruction from incomplete data [39], [43]. It rewards sparsity of the gradient. Since this norm is the L_1-norm of a linear operator, it keeps the optimization problem convex. Regularization is needed for stability but it also contributes to the reduction of artifacts. However, the artifact reduction is mainly achieved by the weights and constraint.

Now we discuss the constraint in the second line of Eqn (2). The symbol $\succeq$ denotes a vector inequality. This is a linear constraint that has not yet been explored in the MAR literature. It is motivated by the knowledge that the metal artifacts are largely due to beam hardening and scatter. These phenomena are not additive noise. Both work in the same direction: the measured attenuation is lower than the ideal (monoenergetic equivalent) attenuation, neglecting noise. Further details about beam hardening are in Appendix A. We discard the non-negativity constraint of previous MAR literature, because the source of the beam hardening and scatter artifacts is addressed by the new constraint. I_P is a diagonal matrix containing a second indicator function for metal.

$$I_P = \mathbf{diag}(p(i)) = \begin{cases} 1 & \sum_{j=1}^{V} a_{ij} I_2(j) > T \\ 0 & \text{otherwise} \end{cases} \tag{5}$$

and

$$I_2(j) = \begin{cases} 1 & X_{Orig}(j) > M_2 \\ 0 & \text{otherwise,} \end{cases} \tag{6}$$

where M_2 is set to 8000 MHU. Since we have noisy measurements, we make an allowance for noise in the constraint. The term σ_p is a vector containing the standard deviation (SD) of the noise estimated per sample. The estimate of the noise in each sample is derived by established methods [2], [44], [45]. Note that we have used two different metal thresholds. For weighting, we use $M_1 = 4000$ MHU, and for the constraint we use $M_2 = 8000$ MHU. This is because we apply the constraint only for high atomic number metals such as copper or iron, for which signifcant beam hardening is expected. We have not applied the constraint for aluminum, because the hardening from aluminum is smaller, so the constraint may not be robust enough against partial volume and blurring from higher atomic number metal objects which may result in lower CT values. The threshold T represents reprojection through 20 voxel widths. Setting $T > 0$ reduces the chance of including voxels wtih high values due to blurring from adjacent voxels, while still including voxels in the interior of high density metal structures whose values are lowered by beam-hardening.

B. Practical Implementation

The description of the implementation is broken up into three subsections, and illustrated in Fig. 1.

1) Identification of metal in the image and sinogram: An FBP reconstruction of the scanner sinogram gives the original image, X_{Orig}. Matlab's standard functions were used for all FBP reconstructions. We use a simple segmentation technique, region growing, to identify image regions containing metal [46]. If a piece of metal has a mass (calculated as CT density times volume) above a minimum mass threshold, its trace in the sinogram is calculated and will be replaced.

2) Construction of the prior-image: The prior-image should represent the attenuation of objects that are dense enough to cause secondary artifacts, such as water, rubber and plastics. In the numerical solution, it is not important to capture textures, to accurately reconstruct non-dense materials such as fabric, or to match the spatial resolution of X_{Orig}. We decrease the size of the problem by solving for a miniature image. The miniature image is reduced by four in each dimension, therefore by a factor of 16 altogether. Building miniature images allows us also to reduce the size of our sinogram. We low-pass filter the projections in view and sample directions, and downsample by a factor of four in the view direction and four in the sample direction. This miniaturization allowed us to overcome computational limitations. The total reduction in size reduces reconstruction time by a factor of 16^3.

We forward project the metal voxels to calculate the attenuation from metal and calculate the weights from Eqn. (3). (Note that we can only approximate the attenuation from metal in this way because beam hardening degrades the reconstruction of the metal itself.) The quadratic program expressed in Eqn. (2) is solved using the Mosek software (Mosek ApS, Denmark) [47]. A was generated by forward projection software [48].

Let the optimal solution be denoted X_C^{mini}. X_C^{mini} can be upsampled to the same size as the original image X_{Orig} and directly used as the prior-image, but we do not do so because although larger structures are preserved, small structures are degraded. Instead, we reconstruct a second image by minimizing the following objective function:

$$\min_x (Ax - b)^T (Ax - b) + \beta_2 ||x||_{TV}. \tag{7}$$

Let the optimal solution to the above equation be X_{LS}^{mini}. In Eqn. (7), there are no weights or constraints. The regularization strength here is $\beta_2 = 0.1\beta$ in Eqn. (2). We use a smaller

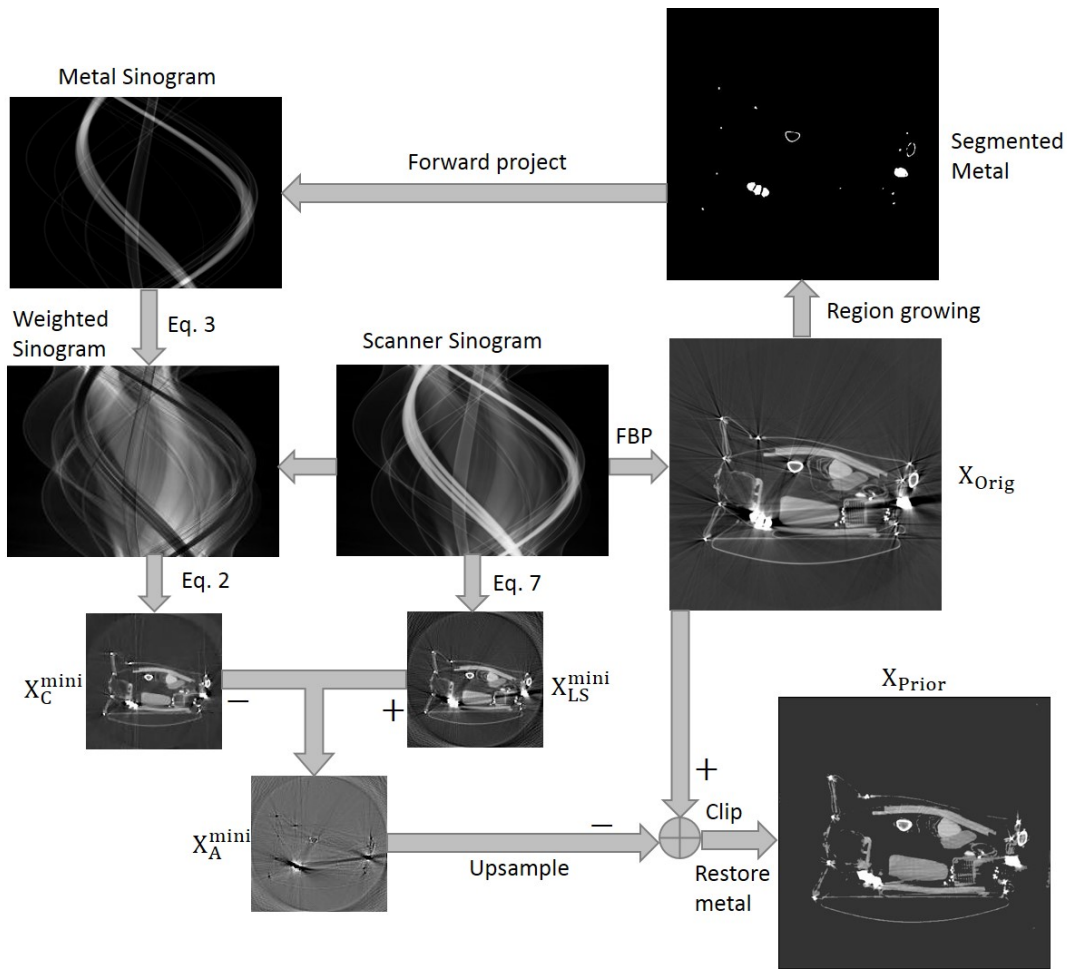

Fig. 1. Pictorial representation of the construction of the prior-image. The flow starts with the scanner sinogram, shown in the center. The optimal solutions to Eqns. (2) and (7) are shown in the smaller images (not to scale).

strength here because we want less interference with the metal artifact structure.

The difference between X_C^{mini} and X_{LS}^{mini} gives an image consisting mainly of artifacts X_A^{mini}.

$$X_A^{mini} = X_{LS}^{mini} - X_C^{mini} \tag{8}$$

We upsample X_A^{mini} using bicubic interpolation to get a full-size artifact only image X_A. Artifacts are removed from X_{Orig} by subtracting X_A:

$$X'_{Prior}(j) = X_{Orig}(j) - X_A(j) \tag{9}$$

The minimization of Eqn. (7) can also be solved by the Mosek solver but we used NESTA [41] because it was faster. NESTA does not allow constraints. There are two more simple but helpful steps. We copy the segmented metal voxels from the original image to the prior-image. This gives us more accurate trace boundaries. More importantly, metal contributes high contrast structures, which should be preserved in the prior-image. Lastly, we clip the small CT values (i.e., below 500 MHU) to the value of air.

$$X_{Prior}(j) = \begin{cases} X'_{Prior}(j) & X'_{Prior}(j) \geq 500 \\ 0 & \text{otherwise.} \end{cases} \tag{10}$$

This removes smaller residual artifacts and any artificial textures created in low density materials such as clothing.

3) Sinogram replacement and final reconstruction:

In this step, (not shown in Fig. 1), we forward project the prior-image, and use a previously published method to replace metal trace data [7]. This method is similar to that in [8] and [13]. The replacement of the metal trace is also called projection or sinogram completion. In this sinogram replacement method, we compute the difference between the original sinogram and the reprojection. We interpolate over the metal trace in these difference projections and get the error. The error is subtracted from the original sinogram, giving us a corrected sinogram. The corrected sinogram is reconstructed with FBP. We have improved upon [7] by fitting the data rather than using linear interpolation, and by blending the corrected with the original sinogram data using Parker weights.

Our original and final image size is 512×512 voxels, and the sinogram size is 1024×720. Due to the downsampling of the sinogram and image, the A matrix size is 46080×16384.

C. Data and Scanner Description

Our data set is obtained from the ALERT group at Northeastern University [49] and consists of scanner data from eight

bags. Bags were packed with various levels of clutter and included an assortment of metallic objects. There were also metallic bag parts. In each bag, there were some objects with uniform attenuation, e.g., contained liquids. The bags were scanned on an electron beam scanner (Imatron, San Francisco, California). The scan technique parameters were 130 kVp, 63 mAs, axial half-scan, 1.5 mm slice thickness, a 475 mm fiield of view, 864 views and 888 samples per view. There was a 1.3-mm increment during the slice acquisition, and a cone angle of 0.3 degrees. These cannot be compensated with a single-slice half-scan. The scanner projection data were corrected for offset (dark current), gain, and beam hardening by water (water calibration) [50]. The correction was water-based because the Imatron is a medical scanner. Although another calibration material for luggage screening may improve overall image quality, to our knowledge there is no industry standard for a substitute. No scatter correction was applied.

D. Evaluation

The MAR algorithm was evaluated visually and by three quantitative measures that measure different aspects of quality. The first measure is based on uniform objects. Existing MAR literature has used phantoms with uniform regions to evaluate the effectiveness of MAR [8], [51]. In our case, each bag contains objects with uniform attenuation, such as contained liquids. In the original images, we manually segment those image regions that we know should be uniform. For each such region, in both the original and MAR images, we characterize the CT number distribution in MHU with minimum, maximum, mean and SD. We also measure the Kolmogorov-Smirnoff (KS2) divergence between the original and MAR images.

The second measure is a sinogram-based error [52]. The sinogram-based error is the L2-norm of the difference of original and synthetic sinograms computed on metal-free samples, normalized by the L2-norm of the original sinogram. The final measure is a reference-free image gradient-based score [52]. The gradient-based score measures the sum of all image gradients. Lower scores correspond to better image quality. We have normalized this score by the value computed on the original images. In addition, we have applied the gradient-based score in 10 pixel-wide bands outside the uniform regions. These bands contain the object boundaries. Since we do not want to lose edges, higher values of this score represent better images.

We evaluate our performance against the iterative projection replacement (IPR) method [12]. We chose this method as a benchmark because of its good results on medical images, and because it makes no assumptions about image content, which makes it more robust than methods specific to medical imaging. We did not compare with the more commonly used benchmark LI-MAR [5] because of its poorer performance than IPR. We computed optimal solutions of the same size as with our method. This made it possible to reconstruct the images on our 16-processor GPU with 96 GB RAM using their preferred solver, NESTA [41], and optimization problem definition. While the authors do not specify image sizes in [12], they state that resolution matching is not required.

We make some improvements to the IPR prior. We copy the original metal into the prior-image, and set any negative voxels to the value of air (0 MHU). These are trivial changes with large improvements in image quality, and are done in most sinogram replacement methods. IPR substitutes the metal traces in the scanner sinogram with reprojected prior-image traces. Substitution may result in discontinuities at the edges of metal traces, hence it may not give good data estimates [13]. Therefore, in addition to IPR results, we compute and present the results of using [7] for data replacement, along with the clipping in Eqn. (10) to further reduce blurring, and call this IPR+.

III. Results and Discussion

We first show one image reconstructed in various ways, in order to qualitatively explain the image quality improvements from our method. Next, we present original and MAR images from more test cases for visual assessment. Third, we show the quantitative results and compare our results with those of a previously published method visually and quantitatively. Finally, we present additional experiments that give a better understanding of the methods.

A. Qualitative Explanation of Image Quality

Fig. 2 shows a 2D image through one bag. The original image with artifacts is in (a) and the MAR image is in (b). The metal artifacts are visually reduced in the MAR image, and this is later confirmed by the quantitative evaluation. For comparison, a regularized WLS image without constraints is shown in Fig. 2(c). This image removes most of the artifacts from the uniform objects. However, the area around the metal continues to show some artifacts. An image representing a benchmark MAR method [5] used in current literature is shown in Fig. 2(d). This image is reconstructed by sinogram replacement without any prior-image (but with identical data fitting, interpolation and blending). The dashed oval shows an example of secondary artifacts, and of the loss of edges. This image is not much better than the original image.

As noted in Section I, previous numeric methods discard all metal data. We demonstrate that discarding all metal traces leads to a loss in image quality. Figs. 3 and 4(a) show the optimal solution image when all metal-containing projection samples are discarded. Fig. 3(a) shows the optimal solution of the unconstrained problem described in [12]. No metal is visible here because metal traces are discarded. If we use this as the prior-image with our own sinogram replacement, we get the image shown in Fig. 3(b). Our metal trace estimation is an improvement over data substitution defined in [12] as discussed in more detail below, but we make this comparison because we wish to compare only the effect of prior-images. In Fig. 3(b), the large circular liquid object is distorted in shape, and dark shadows are present in each of the four uniform objects. The same shadows can be identified in Fig. 3(a).

The effect of the non-negativity constraint along with the deletion of all metal samples is shown by numeric reconstructions in Fig. 4. This experiment demonstrates that there is a loss of image quality when all metal is deleted, and that the

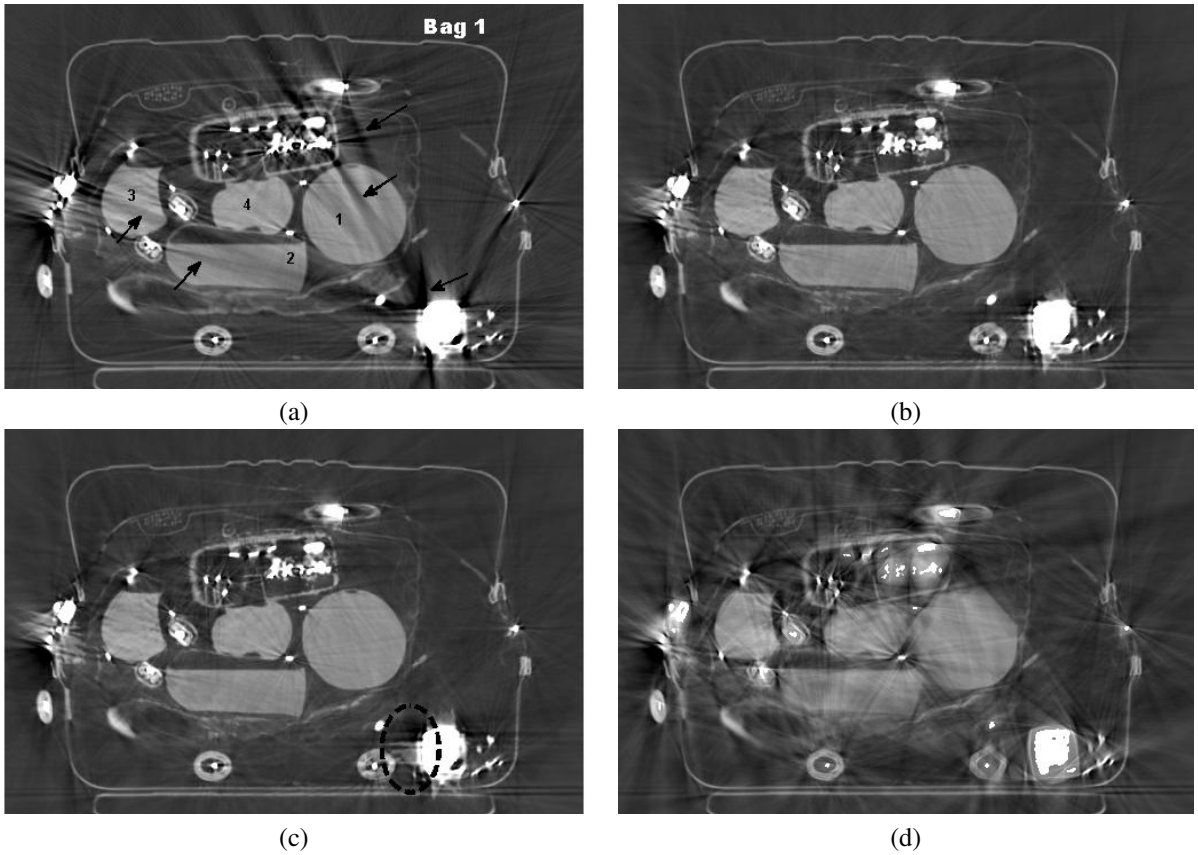

Fig. 2. Image reconstructions of an image from Bag 1. (a) Original image with arrows pointing to the metal artifacts, (b) our method, (c) unconstrained WLS + TV, and (d) sinogram replacement without a prior-image. Window width (WW) = 2500, window-level (WL)=750 MHU. Numbered objects are shown in (a), these denote uniform objects which are quantitatively evaluated in Table I.

non-negativity constraint allows some artifacts to persist, as long as the voxel values do not drop below zero. In Fig. 4(a) all metal data is discarded. Consequently, objects 1, 3, and 4 are fused, and there is dark shading in objects 1 and 3. Weighting instead of discarding metal trace data separates the fused objects as shown in Fig. 4(b). However, the non-negativity constraint still allows dark shading in object 2 in this image. While it is true that CT image values should not be negative, noise, in addition to metal artifacts, can cause negative values in air. The non-negativity constraint is indiscriminate in that it ignores the sources of negative values, while our constraint anticipates where the difference between the measured data and the forward model should be negative.

B. Visual Evaluation

More test cases are shown in Figs. 5 and 6 which contain pairs of original and MAR images. In each test case, the MAR image has less severe artifacts than the original image.

- Bag 2 contains a long piece of metal. MAR removes the curved bright artifact under it and reduces the dark streaks.
- Bag 3 shows a dark streak that lowers amplitude by 200-300 MHU, which could result in objects being split by ATR. The arrow points to a bright artifact, which could result in the water phantom and the sheets below the metal to be merged. The large dark streak, smaller streaks and bright artifact are reduced by MAR.
- Bag 4 has an image with a large amount of metal inside and outside a boom-box. The original image has a dark shading artifact in the uniform object, but the MAR image has reduced shading.
- Bag 5 has some new fine streaks in the uniform object due to the many interpolations needed for the cluster of metal objects at the top and from errors between the scanner and synthetic projections of such small dense objects.
- In Bag 6, the object with fine detail on the right hand side of the suitcase appears to be split by the artifact in the original, but is restored after MAR.

In all cases, we see that large dark artifacts between metal pieces or along the long axes of metal pieces are nearly eliminated along with the bright shadows perpendicular to them. These large artifacts are nearly eliminated while the structure of the contents is preserved, because the prior-image included most of the structures but not the artifacts. The narrower streaks are nearly eliminated simply from the interpolation across the traces of the small metal objects. The metal region may not be well reconstructed because we build our prior-image by de-emphasizing metal projections. Although we copy over the metal voxels, if fine spaces exist between metal voxels exist, they will not be recovered. MAR algorithms can be expected to degrade metal voxels and their neighborhood when

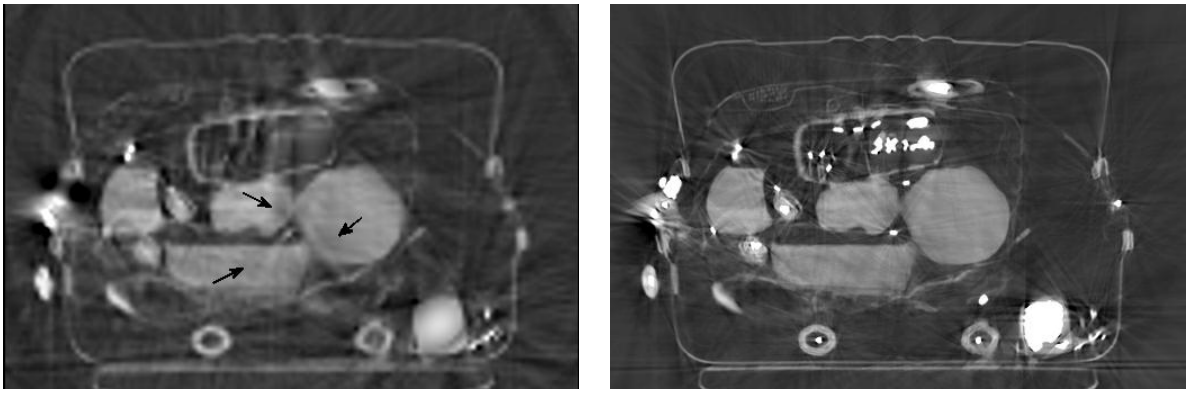

(a) (b)

Fig. 3. Images showing the effect of discarding all metal-contaminated projection samples. (a) The optimal solution of an unconstrained regularized LS solution [12]. (b) MAR image obtained by using the image in (a) as a prior-image (after metal voxels are restored). WW=2500, WL=750.

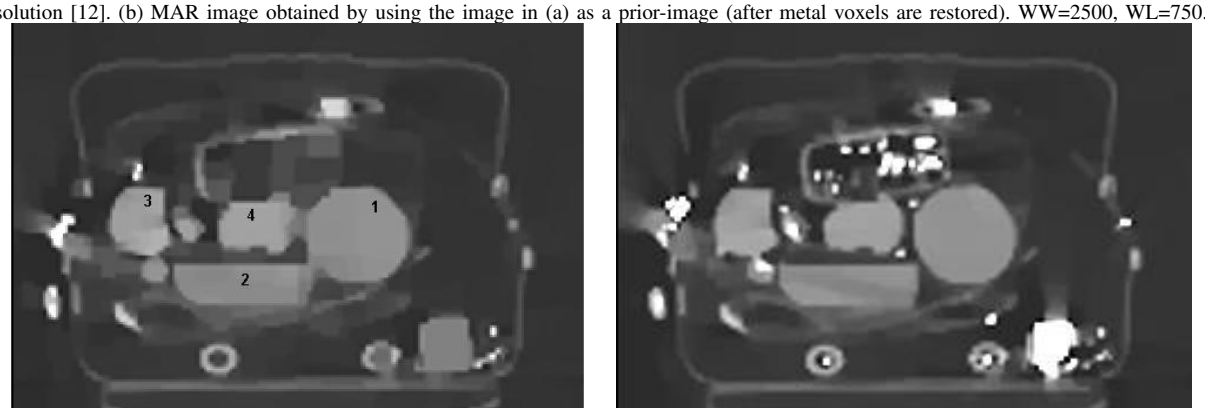

(a) (b)

Fig. 4. Numeric reconstructions (optimal solutions) with the non-negativity constraint. (a) All metal projection data are discarded and the non-negativity constraint is applied. (b) Our weighting function and the non-negativity constraint, but not the constraint in Eqn. (2). WW=2500, WL=750 MHU.

they delete or de-emphasize metal projections.

Although there is an overall improvement with MAR in all images, our algorithm has shortcomings as shown in Fig. 6. A pot (indicated by a white arrow) in Bag 7 throws off beam hardening artifact (horizontal streak from the base of the pot). This is not corrected because the pot was not segmented as metal (its CT density is not high enough, probably because it is thin, made of aluminum, and blurred by the system transfer function). The small water bottle (labeled 1) appears fused to the metal above it in the original image, due to bright, smooth metal artifact. With MAR, this bottle is separated but not well restored. Since it is adjacent to a large piece of metal, when the metal traces are given lower weight, most of the projection samples corresponding to this bottle are also de-emphasized, and in effect, we lose too much data. The larger bottle (labeled 2), however, does not share as much data with the metal object. High amplitude streaks through object 2 are reduced, but it also appears joined to the metal.

Bag 8 contains a laptop and metallic bag parts, which create streaks through the water. After MAR, residual artifact is visible in the water. There is also a loss of resolution along the streaks. The loss of resolution, especially along the streaks, is a phenomenon common to most MAR algorithms [28], [53]. During data replacement, interpolation across metal traces blurs edges along the rays unless the edges are perfectly captured in the prior-image. However, some of the edges in this image are due to soft materials and thin layers, and therefore are not preserved in the prior-image.

C. Quantitative Evaluation

Each bag contains some uniform objects, that are shown numbered in the original images in Figs 2, 5 and 6. The CT number distributions within these objects were measured. The results are given in Table I. The object numbers in the table correspond to the numbering in the original images. The table reveals that the maximum and minimum CT values are closer to the mean value in the MAR images than in the original images. The SD is smaller in the MAR images than the originals for all but one object (object 1 in Bag 7). The KS2 test-statistic is shown in the table column labeled $KS2$. According to the KS2 test, the CT number distributions are different at the 0.05 significance level (p-values not shown). When we consider KS2 along with the SD scores, the KS2 scores tell us that the lower std dev of MAR images is not caused simply by long tails of the CT number distribution. A few uniform objects were scanned separately. Their means were measured and are given in Table I. In the bags, means shift due to metal artifacts and due to clutter. MAR brings the means closer to the ideal values.

Table II shows a comparison of the SDs of uniform objects

Bag	Obj	Min	Max	Mean	Ideal	Std	KS2
Bag 1	O1	155	1296	843		159	0.34
	MO1	713	1080	886		48	
	O2	380	1140	769		133	0.41
	MO2	623	1061	843		65	
	O3	582	1457	988		162	0.15
	MO3	632	1309	1006		114	
	O4	692	1327	1025		79	0.25
	MO4	474	1212	979		72	
Bag 2	O1	513	850	690		41	0.07
	MO1	552	850	687		36	
Bag 3	O1	306	1352	695		201	0.46
	MO1	569	1116	867		101	
	O2	814	2315	1795	1920	164	0.31
	MO2	962	2135	1866		74	
	O3	718	1868	1276		220	0.20
	MO3	959	1460	1260		114	
	O4	358	2546	1092	1004	228	0.24
	MO4	591	2145	1049		121	
	O5	-427	2644	1114		316	0.17
	MO5	60	1624	1131		136	
Bag 4	O1	456	1155	917		111	0.14
	MO1	700	1129	958		65	
Bag 5	O1	553	1108	991	1002	60	0.09
	MO1	737	1135	998		38	
Bag 6	O1	837	1513	1150		106	0.04
	MO1	909	1431	1147		94	
	O2	288	1600	910	1002*	226	0.23
	MO2	371	1357	919		127	
	O3	1187	1568	1337		72	0.24
	MO3	1186	1529	1356		54	
	O4	618	1080	841		90	0.38
	MO4	671	1080	907		72	
Bag 7	O1	862	1954	1244		143	0.69
	MO1	387	1912	992		182	
	O2	-205	1437	935		306	0.52
	MO2	938	1728	1230		113	
Bag 8	O1	269	1229	939	1001	145	0.17
	MO1	504	1138	958		94	

TABLE I

THE MEASURED CT NUMBER DISTRIBUTION IN UNIFORM OBJECTS. IN THE ORIGINAL IMAGES, THESE OBJECTS (OBJ) ARE NUMBERED 1,2 ETC., AND AFTER MAR, THEY ARE NUMBERED M1, M2 ETC. THE SD IS LOWER IN THE MAR IMAGE IN ALL OBJECTS BUT ONE (BAG 7, OBJECT 1). THE AVERAGE SDS WEIGHTED BY OBJECT SIZE ARE 162 AND 87 MHU FOR ORIGINAL AND MAR IMAGES RESPECTIVELY. THE IDEAL VALUE MARKED WITH * WAS NOT AVAILABLE, BUT IS DISTILLED WATER IN A DIFFERENT BOTTLE.

with our MAR and the IPR methods. The mean SD weighted by object volume from IPR is 128, from IPR+ is 117 and from our method is 87 HU. An important finding not represented by uniformity is the distortion of objects in IPR and IPR+ images as shown in Fig. 7. Objects appear to be fused together as a result of their edges being blurred in the prior-image (because all sinogram data containing metal are discarded).

Evaluation with SD alone is insufficient because SD can be lowered just by smoothing. For example, a reconstruction algorithm "$x = 0$" will result in SD being trivially zero. Therefore, we use other measures also. Table III shows the sinogram-based error [52]. This sinogram-based error is intuitive and measures an overall error. In each bag, the error decreases with MAR. The small difference in Bag 1 is likely due to the fact that there are 27 pieces of metal, so much of the sinogram is excluded. The IPR method must have the best scores by definition, because IPR minimizes the same cost that is measured by this error, i.e., the squared error between the original and synthetic sinograms in the metal-free samples.

Bag	Object	StdIPR	StdIPR+	Std.	KS2	KS2+
Bag 1	O1	96	70	48	0.36	0.09
	O2	109	93	65	0.36	0.13
	O3	186	128	114	0.34	0.15
	O4	181	125	72	0.22	0.14
Bag 2	O1	89	82	36	0.30	0.26
Bag 3	O1	129	110	101	0.30	0.17
	O2	134	111	74	0.20	0.14
	O3	134	95	114	0.12	0.30
	O4	127	120	121	0.31	0.22
	O5	165	149	136	0.19	0.11
Bag 4	O1	96	101	65	0.14	0.23
Bag 5	O1	58	43	38	0.22	0.08
Bag 6	O1	187	143	94	0.40	0.23
	O2	143	136	127	0.21	0.10
	O3	64	61	54	0.27	0.27
	O4	130	124	72	0.26	0.15
Bag 7	O1	288	292	182	0.13	0.13
	O2	148	177	113	0.14	0.16
Bag 8	O1	76	102	94	0.29	0.07
Mean		128	116	87		

TABLE II

THE SD IN UNIFORM OBJECTS FOR IPR AND IPR+ AND OUR METHOD, RESPECTIVELY DENOTED STDIPR, STDIPR+ AND -OURS. THE OBJECTS IN EACH IMAGE ARE NUMBERED AS IN THE ORIGINAL IMAGES. THE SYMBOLS KS2 AND KS2+ DENOTE KS2 VALUES THAT COMPARE OUR METHOD AGAINST IPR AND IPR+ RESPECTIVELY.

Bag	Bag 1	Bag 2	Bag 3	Bag 4	Bag 5	Bag 6	Bag 7	Bag 8
Orig	3.18	4.52	4.26	4.10	4.37	3.74	4.75	5.95
MAR	3.02	3.38	3.16	3.32	4.01	2.83	3.78	3.43
IPR	2.72	2.09	2.75	2.62	3.39	2.84	3.12	3.13
IPR+	2.99	4.46	3.26	3.30	3.81	2.88	3.71	3.53

TABLE III

THE SINOGRAM-BASED ERRORS FOR EACH BAG ARE SMALLER AFTER MAR THAN THE ORIGINAL.

Finally, we measure image gradients because the sinogram-based error can suppress errors accumulated through reprojection, and does not fully capture how well resolution is preserved. Table IV shows the gradient-based scores. In each bag, the score decreases with MAR, indicating that the MAR images have less metal artifacts [52]. More importantly, (since the total gradient has the same limitation as SD), when measured only at the boundary of uniform objects, the score is close to that of the original image, indicating that we do not substantially sacrifice edge sharpness to obtain lower SD. The slightly smaller score may be due to a loss of sharpness, or may reflect that the artifacts, which contribute to the total gradient, are reduced. IPR shows the most loss of edge contrast, which matches the visual assessment.

Bag	Bag 1	Bag 2	Bag 3	Bag 4	Bag 5	Bag 6	Bag 7	Bag 8
MAR	0.83	0.73	0.77	0.81	0.87	0.80	0.80	0.81
IPR	0.93	0.72	0.84	0.86	0.92	0.92	0.93	0.84
IPR+	0.80	0.71	0.73	0.77	0.87	0.77	0.76	0.80
MAR	0.94	0.98	0.92	0.95	0.98	0.95	0.91	0.95
IPR	0.89	0.96	0.86	0.91	0.92	0.91	0.88	0.92
IPR+	0.88	0.96	0.87	0.93	0.94	0.90	0.85	0.92

TABLE IV

NORMALIZED SUM OF GRADIENT MAGNITUDES. THE TOP THREE ROWS CONTAIN VALUES COMPUTED FROM THE ENTIRE IMAGE. LOWER SCORES REPRESENT BETTER IMAGE QUALITY. THE BOTTOM THREE ROWS CONTAIN VALUES COMPUTED IN THE BOUNDARY REGIONS. HIGHER SCORES REPRESENT BETTER IMAGE QUALITY.

D. Further analysis

In this section we discuss points that give some more insight into this MAR method.

The LS solution without regularization is equivalent to FBP reconstruction if adequate sampling is present [54]. Therefore, the artifact amplitude and locations are similar in FBP and LS solutions. The numeric solution is influenced by the regularization term, and the FBP solution is influenced by the reconstruction kernel, therefore the FBP and LS solutions are different in details. When we compute the difference of the numeric solutions, we get an image of artifacts, which we subtract from the original image. The prior-image therefore retains the resolution of the original FBP image, and is less influenced by the regularization term than if the optimal solution were used directly.

We chose exponential weights because attenuation is exponential, the weights are smooth and monotonic, and a one-parameter family of weights was easy to tune. The heuristic nature of our weighting motivates the construction of a constraint. The constraint helps to prevent errors from being pushed elsewhere in the image. Fig. 8 shows two images with the weights but without constraints of Eqn.(2). By comparing these images with those of Fig. 5, we see that it is helpful to constrain the solutions. The regularization controls the sparsity of the image gradient. It reduces secondary artifacts that could arise from abrupt changes in weights. Fig. 9 demonstrates the effect of β in Eqn. (2). The allowance for noise provides some flexibility which is helpful when the constraints are too tight. With the current constraint parameter tuning and noise on this dataset, allowance for noise does not make much difference.

We are agnostic about the sinogram replacement technique. However, the technique should be robust enough against small errors in the prior. NMAR [53] interpolates a ratio of the original and synthetic sinograms. When synthetic sinogram samples have small values, this ratio has large errors. Large errors in samples near metal will lead to secondary artifacts. This problem occurs near metallic bag parts of a bag that is not tightly packed, since there is little material to attenuate those rays. Our prior-image thresholding also lowers the amplitude of the synthetic samples. Fig. 10 shows the secondary artifacts. All of our images reconstructed with NMAR have secondary artifacts at least as strong as the image shown. Sinogram preprocessing may help NMAR work with our prior.

We draw a distinction between our method and those that perform sinogram subtraction without a prior-image, exemplified by [55]. The authors find limited improvement in their application and Fig. 11 shows this approach is ineffective in our application. Reprojection of metal voxels cannot accurately quantify the metal due to beam hardening itself, as demonstrated by simulations in [31]. Therefore, subtraction of synthetic projections of metal cannot reverse the beam hardening.

IV. Ongoing Work

There are many areas to explore for further reduction of residual artifacts and preservation of small structures. 1) We can improve the constraints or add to them, e.g., box constraints per image voxel. Another example is that instead of thresholds, alternative criteria may give better results for determining which projections to constrain. 2) We should explore the use of alternate objective functions [56]–[58]. 3) Further research in weighting methods is likely to give better results. We also can explore how to quantify the metal. We used indicator functions on the metal rather than to sum the value of the metal. The reconstructed metal itself is degraded and forward projection cannot reliably quantify it. Poor quantification of metal gives rise to unreliable weights. 4) More sophisticated sinogram replacement may give better image quality e.g., with variational inpainting. 5) Alternate materials for calibration, and scatter correction may improve overall image quality.

Faster optimization is necessary for practical use. The Mosek solver takes about 20 minutes to reconstruct the miniature using the low precision setting. NESTA took under 2 minutes for a tolerance of 10^{-4}. Both are general purpose solvers. A special purpose solver may allow us to reconstruct larger optimal images to better preserve small structures. Or it could be used to obtain practical reconstruction times. In medical imaging, ICD-based solvers are approaching practical reconstruction times for full-size images [59].

Although this method was developed for luggage because of the large amounts of metal and unpredictability of contents, we believe this method can be applied to medical imaging. Refinements and parameter tuning may be necessary. The prior-image based MAR methods in medical CT have shown that it is not necessary to preserve soft-tissue detail in the prior-image, but it is necessary to adequately reconstruct bone, air pockets and high contrast interfaces. The soft tissue details are captured in the final reconstruction.

V. Conclusions

We have developed a new MAR method and tested it on images of luggage with up to 27 pieces of metal. The results of our method show that metal artifacts were significantly reduced based on visual assessment and quantitative evaluation. Our contributions are in three areas. 1) A new formulation of an optimization problem, including projection weighting and a constraint. Methods applicable for luggage scanning, and many MAR methods in general, discard metal projections, but we do not, so that details and contrast are better preserved. We use a constraint that accomodates beam hardening and scatter, and gives better results than the non-negativity constraint of previous literature. 2) The difference of solutions to two different optimization problems removes the effects of mismatched spatial resolution from FBP and optimal solutions, and isolates the artifacts. 3) Miniaturization allows us to directly solve the constrained optimization problem, and subsequent upsampling allows its use in MAR.

VI. Acknowledgements

This work was supported by Lawrence Livermore National Laboratories and the Science and Technology Directorate of the Department of Homeland Security. Scanner data were supplied by the ALERT group at Northeastern University. The

authors thank P. Jin for forward projection software, Dr. T. Partridge for information about the Imatron scanner, and Drs. X. Jiang and C. Crawford for helpful reviews of this work.

Appendix A
Constraint to accomodate beam hardening

In this section we discuss the reason for the linear constraint in Eqn. (2). Monoenergetic attenuation is described by the following equation [60]:

$$I(s,\theta) = I_0 e^{-\int_{s+l\theta\in L}\mu(s+l\theta,E_0)dl} \tag{11}$$

so that the log-attenuation projections are recovered by

$$p(s,\theta) = \int_{s+l\theta\in L}\mu(s+l\theta,E_0)dl = \log\left(\frac{I_0}{I(s,\theta)}\right) \tag{12}$$

The integration here is over the scanned space L between source and detector, s is a vector representing the source position, and θ is a unit vector in the direction from the source position to a detector element.

For a polyenergetic spectrum denoted by $S(E)$, attenuation is described by the following equation [60]:

$$I(s,\theta) = \int S(E)e^{-\int_{s+l\theta\in L}\mu(s+l\theta,E)dl}dE \tag{13}$$

However, the measured log-attenuation projections are still calculated with Eqn. (12). If we normalize I_0 to 1, then $S(E)$ represents a probability mass function for the incident energy. Consider a homogenous object. The expression

$$-\log\int e^{-\mu(E)l}dE \tag{14}$$

is a concave function in the path length l since it is of the -log-sum-exp form [61]. This function includes zero, is non-decreasing and is positive. Therefore, the measured value is always less than the ideal. This justifies our constraint.

References

[1] "Final Report on Algorithm Devlopment for Security Applications," in *Algorithm Development for Security Applications*, M. Silevitch, C. Crawford, and H. Martz, Eds., Boston, 2009.

[2] A. Kak and M. Slaney, *Principles of computerized tomographic imaging*. Philadelphia, PA 19104: SIAM, 1988.

[3] B. D. Man and J. Nuyts, "Metal streak artifacts in X-ray computed tomography: a simulation study," in *Nuclear Science Symposium*, 1998, pp. 1860–1865.

[4] G. Glover and N. Pelc, "An algorithm for the reduction of metal clip artifacts in CT reconstructions," *Medical Physics*, vol. 8, pp. 799–807, 1981.

[5] W. Kalender, R. Hebel, and J. Ebersberger, "Reduction of CT artifacts caused by metallic implants," *Radiology*, vol. 164, no. 2, pp. 576–77, 1987.

[6] S. Zhao, D. D. Robertson, G. Wang, B. Whiting, and K. T. Bae, "X-ray CT metal artifact reduction using wavelets: an application for imaging total hip prostheses." *IEEE Transactions on Medical Imaging*, vol. 19, no. 12, pp. 1238–47, Dec. 2000.

[7] R. Naidu, I. Bechwati, S. Karimi, S. Simanovsky, and C. Crawford, "Method of and system for reducing metal artifacts in images generated by x-ray scanning devices," U.S. Patent 6 721 387, 2004.

[8] M. Bal and L. Spies, "Metal artifact reduction in CT using tissue-class modeling and adaptive prefiltering," *Medical Physics*, vol. 33, no. 8, pp. 2852–2859, Jul. 2006.

[9] C. Golden, S. R. Mazin, F. E. Boas, G. Tye, P. Ghanouni, G. Gold, M. Sofilos, and N. J. Pelc, "A comparison of four algorithms for metal artifact reduction in CT imaging," in *SPIE Medical Imaging*, N. J. Pelc, E. Samei, and R. M. Nishikawa, Eds. International Society for Optics and Photonics, Mar. 2011, p. 79612Y.

[10] E. Meyer, R. Raupach, M. Lell, B. Schmidt, and M. Kachelrieß, "Frequency split metal artifact reduction (FSMAR) in computed tomography." *Medical Physics*, vol. 39, no. 4, pp. 1904–16, Apr. 2012.

[11] F. E. Boas and D. Fleischmann, "Evaluation of two iterative techniques for reducing metal artifacts in computed tomography." *Radiology*, vol. 259, no. 3, pp. 894–902, Jun. 2011.

[12] J. M. Verburg and J. Seco, "CT metal artifact reduction method correcting for beam hardening and missing projections." *Physics in Medicine and Biology*, vol. 57, no. 9, pp. 2803–18, May 2012.

[13] T. Koehler, B. Brendel, and K. Brown, "A New Method for Metal Artifact Reduction in CT," in *The International Conference in X-ray Computed Tomography*, Salt Lake City, Utah, USA, 2011.

[14] R. Alvarez and A. Macovski, "Energy-selective reconstructions in x-ray computerised tomography," *Physics in Medicine and Biology*, vol. 21, no. 5, pp. 733–744, 1976.

[15] B. De Man, J. Nuyts, P. Dupont, G. Marchal, and P. Suetens, "An iterative maximum-likelihood polychromatic algorithm for CT." *IEEE Transactions on Medical Imaging*, vol. 20, no. 10, pp. 999–1008, Oct. 2001.

[16] F. Bamberg, A. Dierks, and K. Nikolaou, "Metal artifact reduction by dual energy computed tomography using monoenergetic extrapolation," *European Radiology*, vol. 21, no. 7, pp. 1424–1429, 2011.

[17] P. Sukovic and N. Clinthorne, "Penalized weighted least-squares image reconstruction for dual energy X-ray transmission tomography," *IEEE Transactions on Medical Imaging*, vol. 19, no. 11, pp. 1075 – 1081, 2000.

[18] H. Xue, L. Zhang, and Y. Xiao, "Metal artifact reduction in dual energy CT by sinogram segmentation based on active contour model and TV inpainting," in *Nuclear Science Symposium Conference Record (NSS/MIC)*, Orlando, FL, 2009, pp. 904–908.

[19] H. Li, L. Yu, X. Liu, J. G. Fletcher, and C. H. McCollough, "Metal artifact suppression from reformatted projections in multislice helical CT using dual-front active contours," *Medical Physics*, vol. 37, no. 10, p. 5155, Sep. 2010.

[20] C. Zhou, Y. Zhao, S. Luo, H. Shi, and L. Zheng, "Monoenergetic imaging of dual-energy CT reduces artifacts from implanted metal orthopedic devices in patients with factures," *Academic Radiology*, vol. 18, no. 10, pp. 1252–1257, 2011.

[21] G. Wang and D. Snyder, "Iterative deblurring for CT metal artifact reduction," *IEEE Transactions on Medical Imaging*, vol. 15, no. 5, pp. 657–664, 1996.

[22] M. Oehler and T. Buzug, "Modified MLEM algorithm for artifact suppression in CT," in *Nuclear Science Symposium Conference Record*, vol. 6, San Diego, CA, 2006, pp. 3511–3518.

[23] R. Murphy, S. Yan, J. O'Sullivan, D. Snyder, B. Whiting, D. Politte, G. Lasio, and J. Williamson, "Pose estimation of known objects during transmission tomographic image reconstruction," *IEEE Transactions on Medical Imaging*, vol. 25, no. 10, pp. 1392–1404, Oct. 2006.

[24] C. Lemmens, D. Faul, and J. Nuyts, "Suppression of metal artifacts in CT using a reconstruction procedure that combines MAP and projection completion," *IEEE Transactions on Medical Imaging*, vol. 28, no. 2, pp. 250–260, 2009.

[25] J. Stayman and Y. Otake, "Model-Based Tomographic Reconstruction of Objects Containing Known Components," *IEEE Transactions on Medical Imaging*, vol. 31, no. 10, pp. 1837–1848, 2012.

[26] T. Sakimoto and K. Nishino, "Metal artifact reduction in tomosynthesis by metal extraction and ordered subset-expectation maximization (OS-EM) reconstruction," in *SPIE Medical Imaging*, 2013, p. 86685M.

[27] J. Rinkel, W. Dillon, and T. Funk, "Computed tomographic metal artifact reduction for the detection and quantitation of small features near large metallic implants: a comparison of published methods," *Journal of Computer Assisted Tomography*, vol. 32, no. 4, pp. 621–629, 2008.

[28] A. Mouton and N. Megherbi, "An experimental survey of metal artefact reduction in computed tomography," *Journal of X-ray Science and Technology*, vol. 21, no. 2, pp. 193–226, 2013.

[29] M. Stille, B. Kratz, J. Müller, N. Maass, I. Schasiepen, M. Elter, I. Weyers, and T. M. Buzug, "Influence of metal segmentation on the quality of metal artifact reduction methods," in *SPIE Medical Imaging*, R. M. Nishikawa and B. R. Whiting, Eds. International Society for Optics and Photonics, Mar. 2013, pp. 86 683C–86 683C–6.

[30] H. Tuy, "A post-processing algorithm to reduce metallic clip artifacts in CT images," *European Radiology*, vol. 3, no. 2, pp. 129–134, 1993.

[31] S. Karimi, P. Cosman, C. Wald, and H. Martz, "Segmentation of artifacts and anatomy in CT metal artifact reduction," *Medical Physics*, vol. 39, pp. 5857–5868, 2012.

[32] J. Wang, S. Wang, Y. Chen, J. Wu, J.-L. Coatrieux, and L. Luo, "Metal artifact reduction in CT using fusion based prior image." *Medical physics*, vol. 40, no. 8, p. 081903, Aug. 2013.

[33] L. Grady, V. Singh, T. Kohlberger, C. Alvino, and C. Bahlmann, "Automatic Segmentation of Unknown Objects, with Application to Baggage Security," in *European Conference on Computer Vision*. Florence, Italy: Springer-Verlag, 2012, pp. 430–444.

[34] M. R. Paudel, M. Mackenzie, B. G. Fallone, and S. Rathee, "Evaluation of normalized metal artifact reduction (NMAR) in kVCT using MVCT prior images for radiotherapy treatment planning," *Medical Physics*, vol. 40, no. 8, p. 081701, Jul. 2013.

[35] I. A. Elbakri and J. A. Fessler, "Statistical image reconstruction for polyenergetic X-ray computed tomography." *IEEE Transactions on Medical Imaging*, vol. 21, no. 2, pp. 89–99, Feb. 2002.

[36] ——, "Segmentation-free statistical image reconstruction for polyenergetic x-ray computed tomography with experimental validation," *Physics in Medicine and Biology*, vol. 48, no. 15, pp. 2453–2477, Aug. 2003.

[37] X. Zhang, J. Wang, and L. Xing, "Metal artifact reduction in x-ray computed tomography (CT) by constrained optimization," *Medical Physics*, vol. 38, no. 2, p. 701, 2011.

[38] Y. Zhang, H. Yan, X. Jia, J. Yang, S. Jiang, and X. Mou, "A hybrid metal artifact reduction algorithm for x-ray CT," *Medical Physics*, vol. 40, p. 041910, 2013.

[39] E. Y. Sidky and X. Pan, "Image reconstruction in circular cone-beam computed tomography by constrained, total-variation minimization." *Physics in Medicine and Biology*, vol. 53, no. 17, pp. 4777–807, Sep. 2008.

[40] Y. Nesterov, "Smooth minimization of non-smooth functions," *Mathematical Programming*, vol. 103, no. 1, pp. 127–152, 2005.

[41] S. Becker, J. Er, and E. J. C. Es, "Nesta: a fast and accurate first-order method for sparse recovery ," California Institute of Technology, Tech. Rep. 3, 2009.

[42] J. Fessler, "Penalized weighted least-squares image reconstruction for positron emission tomography," *IEEE Transactions on Medical Imaging*, vol. 13, no. 2, pp. 290–300, 1994.

[43] G.-H. Chen, J. Tang, and S. Leng, "Prior image constrained compressed sensing (PICCS): A method to accurately reconstruct dynamic CT images from highly undersampled projection data sets," *Medical Physics*, vol. 35, no. 2, p. 660, Jan. 2008.

[44] A. Papoulis and S. U. Pillai, *Probability, Random Variables and Stochastic Processes*, 4th ed. McGraw-Hill Europe, 2002.

[45] J. Dobbs and H. Weedon, "Normalization of tomographic image data," U.S. Patent 5 680 427, 1996.

[46] R. Gonzalez, R. Woods, and S. Eddins, *Digital image processing using MATLAB*, 1st ed. Pearson, 2009.

[47] E. Anderson and K. Anderson, "The MOSEK interior point optimizer for linear programming: an implementation of the homogeneous algorithm," 2013.

[48] P. Jin, S. J. Kisner, T. Frese, and C. A. Bouman, "Model-based iteartive reconstruction (MBIR) software for X-ray CT," Nov 2013, available from http://engineering.purdue.edu/˜bouman.

[49] C. Crawford and S. Song, "Scanning Requirement Specification for the ALERT Reconstruction Initiative (Task Order 3)," Awareness and Localization of Explosives-Related Threats (ALERT), Tech. Rep., 2013.

[50] "Research and Development of Reconstruction Advances in CT-based Object Detection Systems," in *New Methods for Explosive Detection for Aviation Security*, C. Crawford, H. Martz, and M. Silevitch, Eds. Boston: Awareness and Localization of Explosives-Related Threats (ALERT), 2013, pp. 390–397.

[51] J. F. Williamson, B. R. Whiting, J. Benac, R. J. Murphy, G. J. Blaine, J. A. OSullivan, D. G. Politte, and D. L. Snyder, "Prospects for quantitative computed tomography imaging in the presence of foreign metal bodies using statistical image reconstruction," *Medical Physics*, vol. 29, no. 10, p. 2404, Sep. 2002.

[52] B. Kratz, S. Ens, J. Muller, and T. M. Buzug, "Reference-free ground truth metric for metal artifact evaluation in CT images," *Medical Physics*, vol. 38, no. 7, p. 4321, Jun. 2011.

[53] E. Meyer, R. Raupach, M. Lell, B. Schmidt, and M. Kachelriess, "Normalized metal artifact reduction (NMAR) in computed tomography." *Medical Physics*, vol. 37, no. 10, pp. 5482–93, Oct. 2010.

[54] F. O'Sullivan, Y. Pawitan, and D. Haynor, "Reducing negativity artifacts in emission tomography: post-processing filtered backprojection solutions," University of Washington, Tech. Rep., 1993. [Online]. Available: http://www.stat.washington.edu/research/reports/1993/tr245.pdf

[55] Y. Takahashi, S. Mori, T. Kozuka, K. Gomi, T. Nose, T. Tahara, M. Oguchi, and T. Yamashita, "Preliminary study of correction of original metal artifacts due to I-125 seeds in postimplant dosimetry for prostate permanent implant brachytherapy," *Radiation Medicine*, vol. 24, no. 2, pp. 133–138, Feb. 2006.

[56] R. Tibshirani, "Regression shrinkage and selection via the lasso," *Journal of the Royal Statistical Society. Series B*, vol. 58, no. 1, pp. 267–288, 1996.

[57] R. Chartrand and W. Yin, "Iteratively reweighted algorithms for compressive sensing," in *IEEE International Conference on Acoustics, Speech and Signal Processing*, 2008.

[58] H. Zou and T. Hastie, "Regularization and variable selection via the Elastic Net," *Journal of the Royal Statistical Society, Series B*, vol. 67, no. 2, pp. 301–320, 2005.

[59] J.-B. Thibault, K. D. Sauer, C. A. Bouman, and J. Hsieh, "A three-dimensional statistical approach to improved image quality for multislice helical CT," *Medical Physics*, vol. 34, no. 11, p. 4526, Oct. 2007.

[60] J. Hsieh, *Computed tomography: Principles, Design, Artifacts, and Recent Advances*, 2nd ed. SPIE–The International Society for Optical Engineering, 2009.

[61] S. Boyd and L. Vandenberghe, *Convex optimization*. Cambridge University Press, 2004.

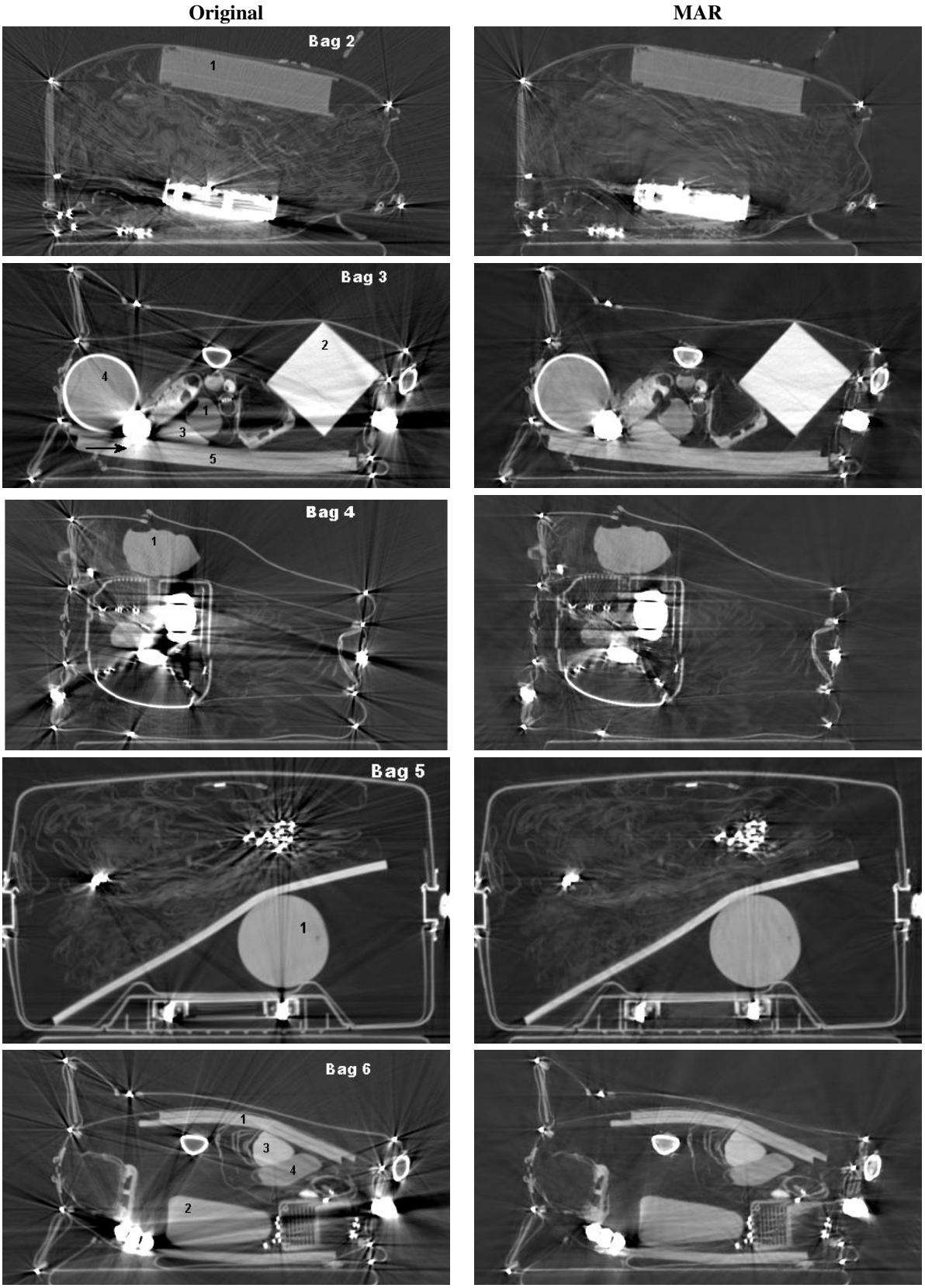

Fig. 5. Images showing a variety of objects, metals and configurations. Each row shows one test case. Original images are shown on the left, and MAR images are on the right. The numbered objects in the original images are uniform objects that are numerically evaluated in Table I. The black arrow in Bag 3 indicates an example of a bright metal artifact. WL/WW (HU) for Bag 1,2,4,6 = 750/2500, for Bag 3 = 850/2300, and for Bag 5 = 750/2100.

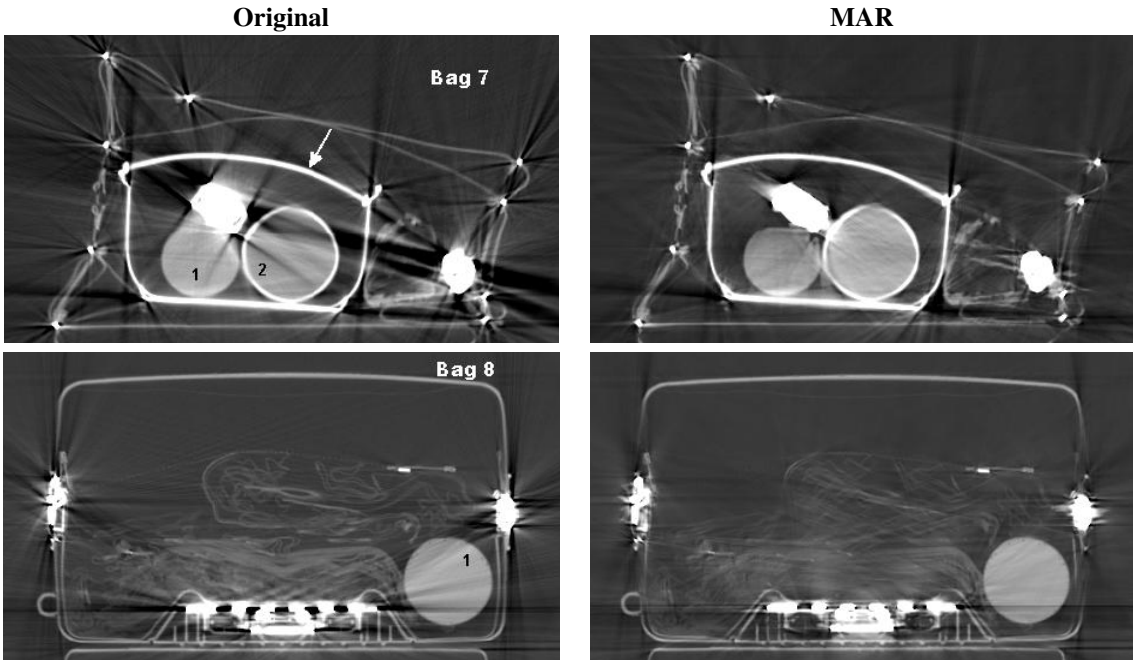

Fig. 6. Original and MAR images showing some shortcomings of our method. WL/WW (HU) Bag 7: 800/2400, Bag 8: 650/2300.

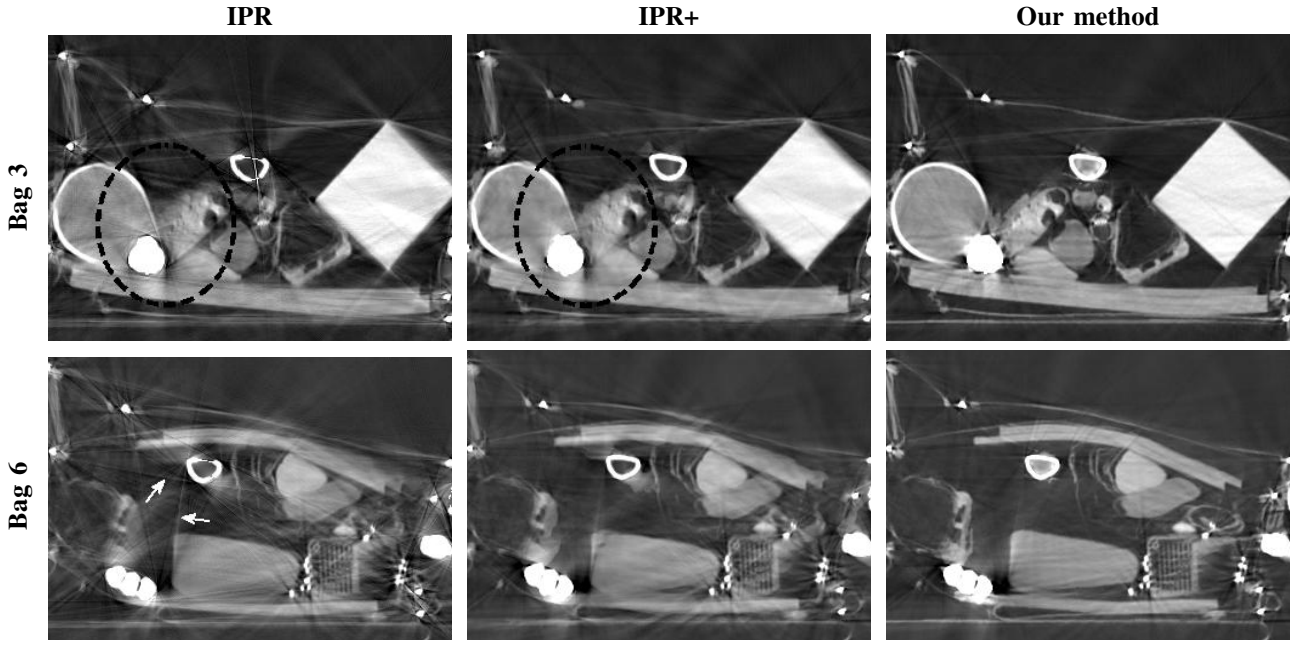

Fig. 7. Comparison of IPR, IPR+ and our method on Bags 3 (top row) and 6 (bottom row). IPR shows a loss of edges e.g., inside the dashed oval, IPR+ shows a small improvement over IPR, and our method shows the best restoration of edges. In the bottom row IPR image, arrows point to the streak artifacts from the substitution of reprojected prior-image samples for the original sinogram samples. WL/WW Bag 3: 850/2300 Bag 6: 750/2500.

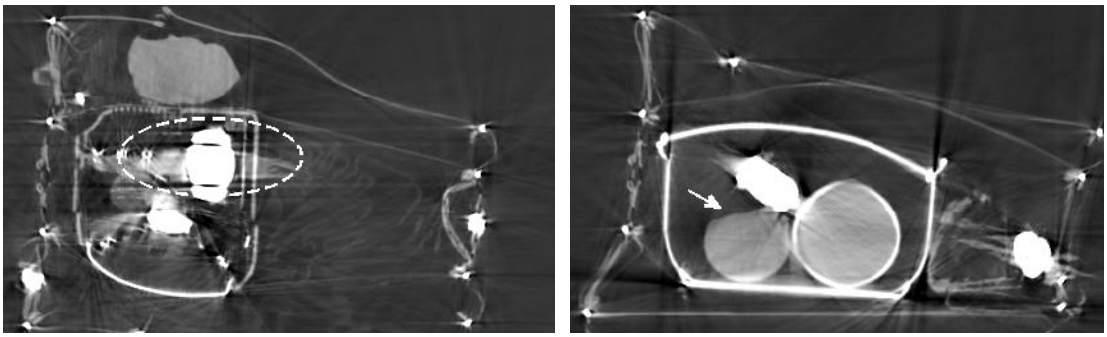

Fig. 8. More images with the weights but not the constraints of Eqn. (2). WL/WW =750/2500. The abrupt cutting off of the water is caused by the clipping step in the generation of the prior-image.

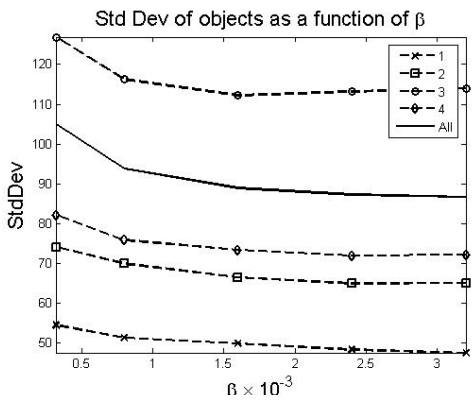

Fig. 9. The effect of varying β in Eqn. (2). The first four objects of Bag 1 are shown by colored lines and the weighted mean of all objects in all bags is shown by the black line.

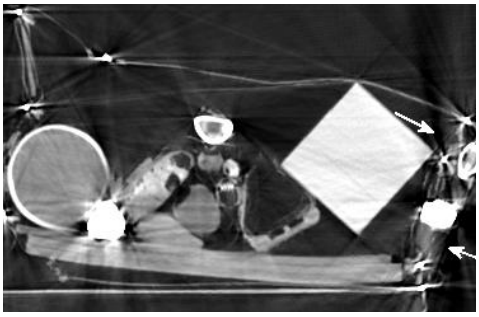

Fig. 10. Sinogram replacement by NMAR. Secondary artifacts are indicated by white arrows. WL/WW = 850/2300.

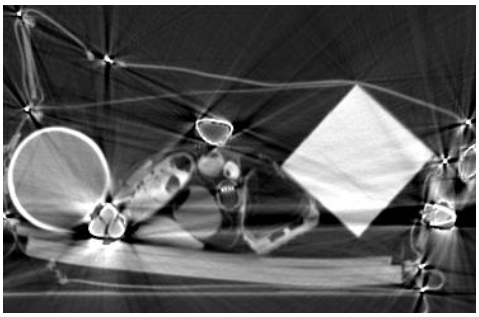

Fig. 11. Sinogram subtraction without a prior-image. WL/WW = 850/2300.